Impact of Ocean Data Assimilation on Climate Predictions with ICON-ESM

H. Pohlmann[1], S. Brune[2], K. Fröhlich[3], J. H. Jungclaus[4], C. Sgoff[3], and J. Baehr[2]

[1]Deutscher Wetterdienst, Hamburg, Germany

[2]Center for Earth System Research and Sustainability, University of Hamburg, Hamburg, Germany

[3]Deutscher Wetterdienst, Offenbach, Germany

[4]Max Planck Institute for Meteorology, Hamburg, Germany

Corresponding author: Holger Pohlmann (holger.pohlmann@dwd.de)

Key Points:

- Development of an ocean data assimilation scheme for the next generation of seasonal to decadal climate predictions at DWD
- High predictability on decadal timescales is confirmed for sea surface temperature and oceanic heat content especially in the North Atlantic
- High predictability on seasonal timescales is confirmed in the tropics in variables related to the El Niño/Southern Oscillation phenomenon

Abstract

We develop a data assimilation scheme with the Icosahedral Non-hydrostatic Earth System Model (ICON-ESM) for operational decadal and seasonal climate predictions at the German weather service. For this purpose, we implement an Ensemble Kalman Filter to the ocean component as a first step towards a weakly coupled data assimilation. We performed an assimilation experiment over the period 1960-2014. This ocean-only assimilation experiment serves to initialize 10-year long retrospective predictions (hindcasts) started each year on 1 November. On multi-annual time scales, we find predictability of sea surface temperature and salinity as well as oceanic heat and salt contents especially in the North Atlantic. The mean Atlantic Meridional Overturning Circulation is realistic and the variability is stable during the assimilation. On seasonal time scales, we find high predictive skill in the tropics with highest values in variables related to the El Niño/Southern Oscillation phenomenon. In the Arctic, the hindcasts correctly represent the decreasing sea ice trend in winter and, to a lesser degree, also in summer, although sea ice concentration is generally much too low in both hemispheres in summer. However, compared to other prediction systems, prediction skill is relatively low in regions apart from the tropical Pacific due to the missing atmospheric assimilation. In addition, we expect a better fine-tuning of the sea ice and the oceanic circulation in the Southern Ocean in ICON-ESM to improve the predictive skill. In general, we demonstrate that our data assimilation method is successfully initializing the oceanic component of the climate system.

Plain Language Summary

The Icosahedral Non-hydrostatic Earth System Model (ICON-ESM) became available recently. The German weather service plans to use the ICON model for operational decadal and seasonal climate predictions. We develop a data assimilation at first for the ocean component that integrates ocean temperature and salinity observations into ICON-ESM in order to start decadal and seasonal climate predictions. We assess the quality of our system with retrospective predictions over the period 1960-2014. We find decadal predictability of the ocean surface temperature and heat content globally and especially in the North Atlantic. Moreover, we find seasonal predictability for variables like sea surface height, surface temperature, air pressure and precipitation particularly in the tropical Pacific. The next step of the data assimilation would be

the additional assimilation of atmospheric observations. As a consequence of the missing atmospheric assimilation in our system, the prediction skill is relatively low in the extratropics. Moreover, a more realistic sea ice cover in ICON-ESM could also improve the predictability at the poles. With the implementation of the oceanic data assimilation into ICON-ESM, the first step towards our next-generation decadal and seasonal prediction system is successfully accomplished.

1 Introduction

The German Meteorological Service "Deutscher Wetterdienst" (DWD) plans to update its currently used climate model for operational seasonal and decadal climate predictions from the Max-Planck-Institute Earth System Model (MPI-ESM) to the Icosahedral Non-hydrostatic Model (ICON; Zängl et al., 2015). ICON is a joint development between DWD, Max Planck Institute for Meteorology (MPI-M), the Karlsruhe Institute for Technology (KIT), the German Climate Computing Center (DKRZ) and other institutions in Germany and Switzerland. The ICON-Earth System Model (ICON-ESM; Jungclaus et al., 2022) has become available recently. We develop - as a first step towards a weakly coupled assimilation - a data assimilation scheme for the oceanic component.

Decadal climate prediction (Smith et al., 2019) is a relatively new field and research activities are supported by the Decadal Climate Prediction Project (DCPP) of the World Climate Research Program (WCRP), which is contributing to the Coupled Model Intercomparison Project (CMIP) phase 5 (CMIP5; Taylor et al., 2012) and phase 6 (CMIP6; Boer et al., 2016). Following an initiative of WCRP's Grand Challenge on Near Term Climate Prediction (Kushnir et al., 2019), decadal climate predictions are coordinated by the Lead Centre for Annual-to-Decadal Climate Prediction (LC ADCP) of the World Meteorological Organization (WMO). About a dozen global producing centers and other contributing centers publish decadal climate predictions in this framework (Hermanson et al., 2022).

Seasonal climate predictions, on the other hand, are well established. The WMO Lead Centre for Long-Range Forecast Multi Model Ensemble (LC LRFMME) and the WCRP's Climate System

Historical Forecast Project (CHFP; Tompkins et al., 2017) organize seasonal climate prediction activities. Another platform for coordinated seasonal predictions is established by the European Union's COPERNICUS program (https://climate.copernicus.eu). The Working Group on Seasonal to Interannual Prediction (WGSIP) has changed its name recently to the Working Group on Subseasonal to Interdecadal Prediction (WGSIP) to combine the efforts on the two time-scales.

Most of the seasonal and decadal climate prediction systems nowadays use a weakly coupled data assimilation, i.e. data assimilation is applied to each component of the climate system separately. Examples for ocean-only initializations are from the beginning of decadal climate predictions (e.g., Keenlyside et al., 2008; Pohlmann et al., 2009; Dunstone, 2010; Swingedouw et al., 2013). Strongly coupled data assimilation, i.e. a common data assimilation for all climate components, might reduce the imbalances between the components caused by the weakly coupled data assimilation further (Penny et al., 2019). Eventually, we are planning a strongly coupled seasonal to decadal data assimilation system. The assimilation of the oceanic component with ICON-ESM is our first step to approach this aim.

A multi-initialization comparison (Polkova et al., 2019) with our previous climate model MPI-ESM has shown best results for the Ensemble Kalman Filter (EnKF) method of the Parallel Data Assimilation Framework (PDAF; Nerger & Hiller, 2013). With this method, we assimilate temperature and salinity profiles from observations into ICON-ESM over the past ca. 55 years to obtain initial conditions for the decadal hindcast simulations. Evidently, a model-consistent initialization strategy avoids some of the problems emerging from a combination of employing two different (ocean) models (Brune et al., 2018), e.g. as has been the case in DWD's previous operational seasonal (Fröhlich et al., 2021) and decadal (Pohlmann et al., 2019) prediction systems, which were initialized from an oceanic reanalysis product.

For high quality climate predictions, it is necessary to preserve the atmosphere-ocean feedback, a task that is not easy to sustain (Brune & Baehr, 2020). With our approach of initializing only the oceanic part, we aim to answer the question for which part of the climate system, that is, with a focus on the ocean itself or the atmosphere by feedback, this method already yields realistic

predictions, and which parts remain to be improved. We organize this paper as follows: In chapter 2, we introduce the experiments and methods and we present our analysis in chapter 3. In chapter 4, we conclude with a summary and discussion of our results.

2 Method

We employ ICON-ESM in the configuration used for the CMIP6 historical simulations (Jungclaus et al., 2022) using transient external forcing from the CMIP6 (Eyring et al., 2016). ICON-ESM consists of the components ICON-Atmosphere (Giorgetta et al., 2018; Crueger et al., 2018), ICON-Ocean (Korn, 2017), ICON-Land based on the Jena Scheme for Biosphere Atmosphere Coupling in Hamburg (JSBACH; Reick et al., 2021) and ICON-Biogeochemistry based on the Hamburg Ocean Carbon Cycle (HAMOCC; Maerz et al., 2020). Ocean and atmosphere are coupled with the "Yet-Another-Coupler" (YAC; Hanke et al., 2016). We use the ICON-ESM at a resolution of 160 km (R2B4) in the ICON-Atmosphere and 40 km (R2B6) in the ICON-Ocean. Jungclaus et al. (2022) have evaluated the Diagnosis, Evaluation, and Characterization of Klima (DECK) simulations with ICON-ESM against observations and find that the mean state and variability is in general similar to other climate models from the CMIP5 and CMIP6.

We produce retrospective decadal climate predictions (hindcasts) with ICON-ESM following the Decadal Climate Prediction Project protocol-A (DCPP-A; Boer et al., 2016). In a first step, we produce an ensemble of 10 assimilation runs with the PDAF EnKF (Nerger & Hiller, 2013) over the period 1960-2014. Monthly ocean temperature and salinity profiles from the EN.4.2.1 data set (Good et al., 2013) are assimilated into ICON-ESM, which is then integrated to the next assimilation step a month later, when the cycle is repeated (Fig. 1). In a second step, we initialize an ensemble of 10 decadal hindcast simulations from the (10) assimilation runs started in each year on the first of November.

The PDAF EnKF offers various parameter settings. In our oceanic assimilation implementation with PDAF EnKF we use a localized singular evolutive interpolated Kalman filter (SEIK; Pham, 2001; Nerger & Hiller, 2013). The horizontal localization range determines the spread of the

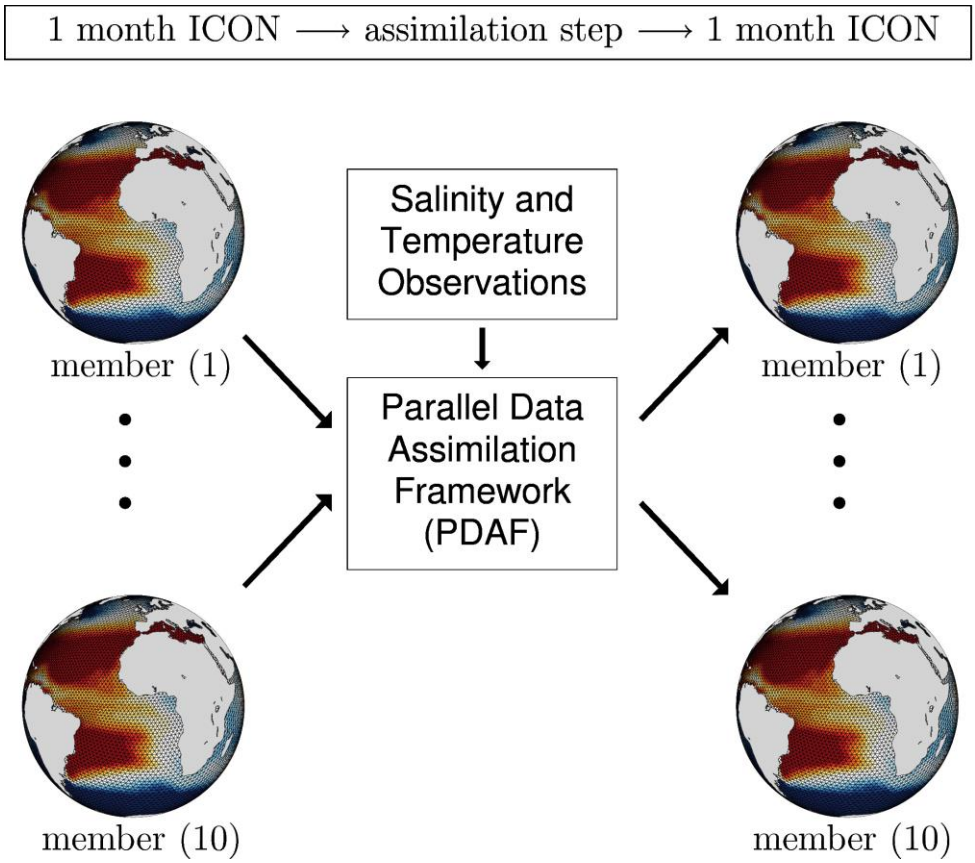

Figure 1. Schematic of the data assimilation. The PDAF Ensemble Kalman Filter assimilates once a month oceanic salinity and temperature profiles into ICON-ESM. The assimilation step is followed by a one-month ICON-ESM run with 10 ensemble members. The procedure is repeated in the next assimilation cycle. This way, the assimilation run is performed over the period 1960-2014 and provides the initial conditions for the decadal hindcast simulations.

temperature and salinity observations to neighboring grid cells and the error range determines the decay of the SST observations. We use no vertical spread of the observations and let the climate model transport the information during the relatively long assimilation step of one month. Based on our experience from previous experiments (Brune et al., 2015), we choose in the present study a local range of 5° and the error range of 1 K and 1 PSU for the temperature and salinity, respectively.

In the following chapter, we analyze the hindcasts with respect to their lead-time dependent prediction skill. While many different skill metrics exist, we choose the Pearson's correlation coefficient (Wilks, 2011) because of its independence on the bias of the hindcasts. Eventually,

post-processing can correct the biases in the climate predictions (Pasternack et al., 2018). We define the lead-time l dependent correlation coefficient cor as

$$cor_l = \frac{\sum_{i=1}^{n}(x_{il}-\bar{x}_l)(y_{il}-\bar{y}_l)}{\sqrt{\sum_{i=1}^{n}(x_{il}-\bar{x}_l)^2}\sqrt{\sum_{i=1}^{n}(y_{il}-\bar{y}_l)^2}} \quad (1)$$

with x represents the ensemble mean hindcast variable of interest and y represents the observed value; i.e. their covariances divided by the product of their standard deviations. Correlation values close to one express a perfect prediction, values around zero mean no prediction skill and negative values indicate an anti-relation between the prediction and observation. We estimate the significance of the correlation values with a student's t-test (Wilks, 2011). To estimate the decadal prediction skill, we analyze annual means for different lead-years (ly). We start the decadal hindcasts on the first of November in each year. Ly1 represents the average over the following calendar year, starting January first hence the last complete year is ly9. We also analyze seasonal prediction skill for lead months (lm) 2-4, which represents the average over December, January and February (DJF) of our hindcasts.

3 Results

3.1 Decadal predictability

Sea surface temperature (SST) variability of ICON-ESM hindcasts exhibits high correlation values with observations from the Hadley Centre Sea Ice and Sea Surface Temperature data set (HadISST; Rayner et al., 2003) over the globe for ly1 (Fig. 2a) and averages over ly1-5 (Fig. 2c). We find high prediction skill in the Atlantic, Indian Ocean and western Pacific, while in parts of the eastern Pacific predictability is low. The comparison of our results with the verification of other models from the LC ADCP (https://hadleyserver.metoffice.gov.uk/wmolc/; Hermanson et al., 2022) shows that the skill in our system is lower in the subtropical gyres of the Pacific and parts of the Southern Oceans and elsewhere competitive.

Some of the regions with high SST prediction skill retain high correlation values also for the upper 700m oceanic heat content (HC-700m), referenced against observations from the Frontier

Research System for Global Change (Ishii et al., 2006), but the regions with significant predictive skill are much smaller for averages over ly1 as well as ly1-5 (Fig. 2b, d). At least some of the areas with low prediction skill of SST and HC-700m can be attributed to the missing atmospheric data assimilation in our system. The wind has a strong influence on the predictability by its impact on ocean dynamics and mixed layer depths (Thoma et al., 2015). Another source of prediction skill from the atmosphere is the air temperature that is directly influencing the temperature of the ocean by heat fluxes. Other atmospheric sources of predictability stem from effects that are more indirect such as precipitation, cloud effects on radiation, evaporation, etc.

We further analyze the North Atlantic SST and HC-700m as the average over the region 60°W-10°W, 50°N-60°N, where we found high predictive skill in our previous prediction system (Kröger et al., 2018). The time series of the observed North Atlantic SST and HC-700m show a low-frequency modulation with low values in the period 1970-1995 and high values thereafter

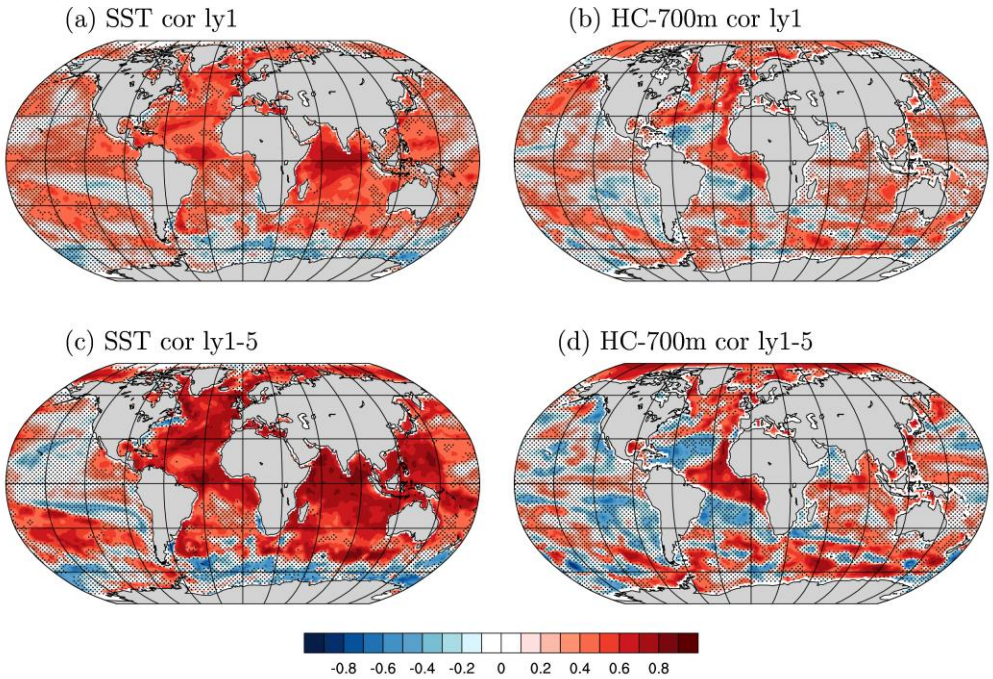

Figure 2. Correlation of (a, c) sea surface temperature (SST) and (b, d) upper 700m heat content (HC-700m) from the ICON-ESM hindcasts with observations (HadISST and Ishii, respectively) for lead-years 1 (a, b) and 1-5 (c, d). The correlations are based on averages of 10 ensemble members over the period (a, c) 1961-2015 and (b, d) 1961-2012, respectively. Stippling indicates regions with non-significant values at the 95% level according to a t-test.

(Fig. 3a, b). The hindcasts with ly1 and averages over ly1-5 follow the observed signal and the correlation coefficients are statistically significant. For North Atlantic SST the correlation values are 0.78 and 0.86 for ly1 and ly1-5, respectively. Additionally, for North Atlantic HC-700m the correlation values are 0.77 and 0.74 for ly1 and ly1-5, respectively.

Next, we give an overview of the correlation values for all possible periods with different start and end lead years (Fig. 3c, d). The idea to display the correlation values in this format was

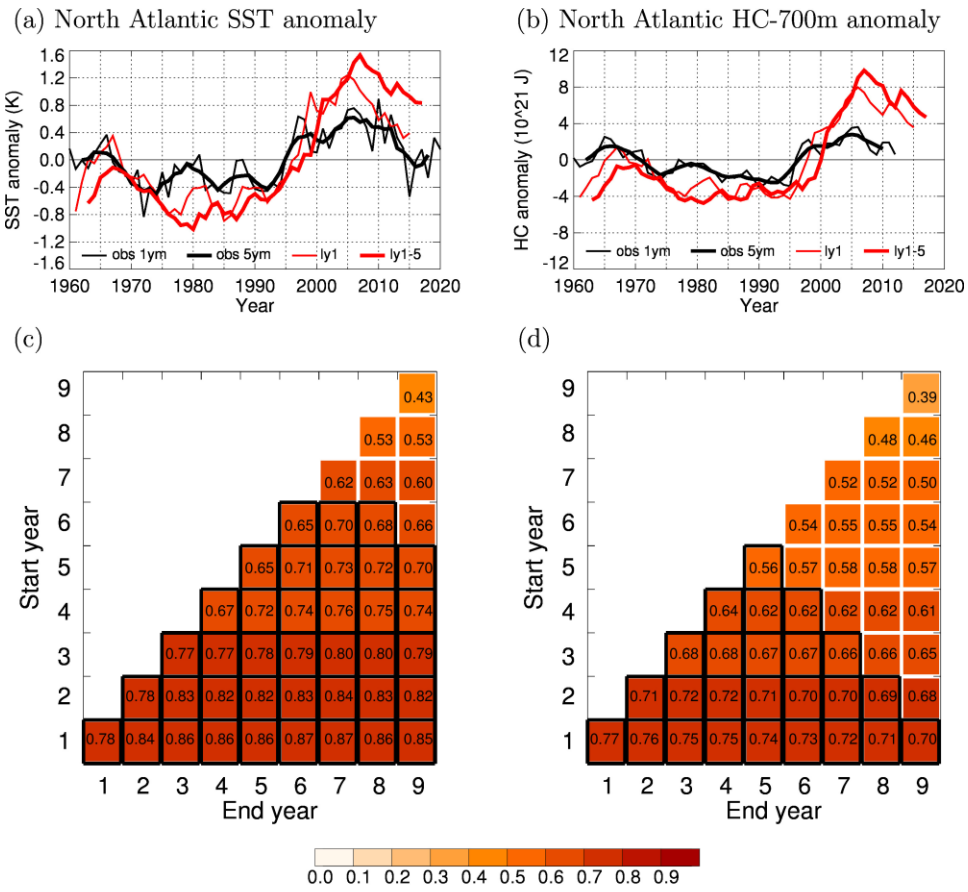

Figure 3. Time series of ensemble and North Atlantic mean (60°W-10°W, 50°N-60°N) (a) sea surface temperature (SST) and (b) upper 700 m heat content (HC) anomalies from ICON-ESM hindcasts (red) and observations (HadISST and Ishii, respectively, black). The time-series of the observations are shown for annual (thin) and 5 year-running means (thick), and the hindcasts for lead-year 1 (thin) and lead-years 1-5 (thick). The diagrams below display the correlation coefficients for different lead-year ranges defined by the start and end years of the time-series for the North Atlantic SST (c) and HC-700m (d). Framed tiles indicate significant values at the 95% level according to a t-test.

204 introduced by Athanasiadis et al. (2020) where it was applied to decadal predictability of
205 blocking and North Atlantic Oscillation. For North Atlantic SST, highest correlation values
206 (cor=0.87) are present for ly1-6, ly1-7 and ly1-8 and the correlation remains statistically
207 significant up to ly6-8 and ly5-9. For North Atlantic HC-700m the highest correlation value
208 (cor=0.81) is present for ly1 and the correlation is significant up to ly1-7.
209

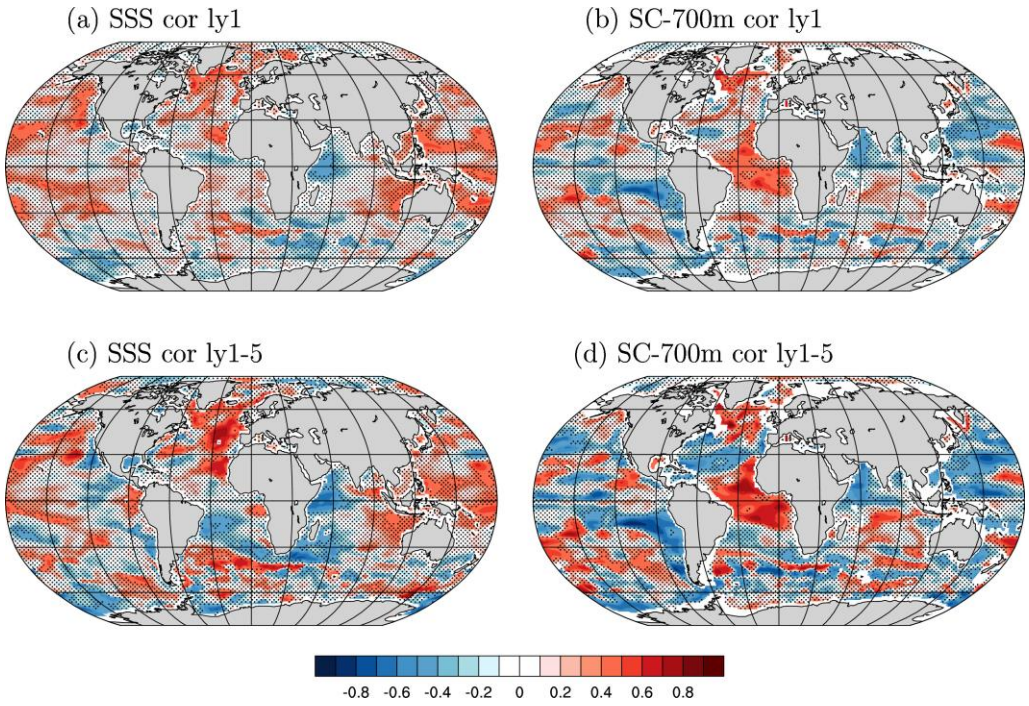

Figure 4. Correlation of (a, c) sea surface salinity (SSS) and (b, d) upper 700m salt content (SC-700m) from the ICON-ESM hindcasts with observations (Ishii) for lead-years 1 (a, b) and 1-5 (c, d). The correlations are based on averages of 10 ensemble members over the period 1961-2012. Stippling indicates regions with non-significant values at the 95% level according to a t-test.

The sea surface salinity (SSS) variability of the ICON-ESM hindcasts exhibits high correlation values with observations from the Frontier Research System for Global Change (Ishii; Ishii et al., 2006) in the North Atlantic and central tropical and subtropical Pacific for averages over the ly1 (Fig. 4a) and ly1-5 (Fig. 4c) while elsewhere the prediction skill is low. The upper 700m oceanic salt content (SC-700m) shows high correlation values with observations from the Frontier Research System for Global Change (Ishii et al., 2006) in the North Atlantic and tropical Atlantic (Fig. 4b, d). Similar to the SSS, the SC-700m prediction skill is low apart from these regions.

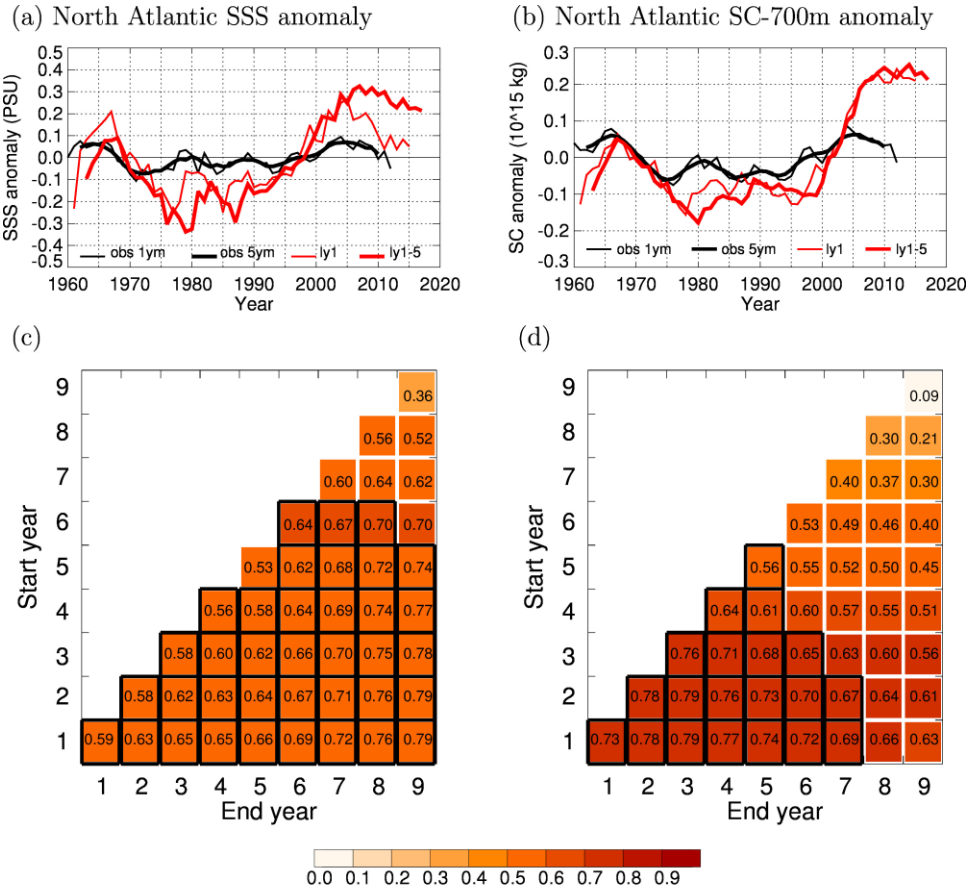

Figure 5. Time series of ensemble and North Atlantic mean (60°W-10°W, 50°N-60°N) (a) sea surface salinity (SSS) and (b) upper 700 m salt content (SC) anomalies from ICON-ESM hindcasts (red) and observations (Ishii, black). The time-series of the observations are shown for annual (thin) and 5 year-running means (thick), and the hindcasts for lead-year 1 (thin) and lead-years 1-5 (thick). The diagrams below display the correlation coefficients for different lead-year ranges defined by the start and end years of the time-series for the North Atlantic SSS (c) and SC-700m (d). Framed tiles indicate significant values at the 95% level according to a t-test.

Salinity observations are sparser than temperature observations and SSS observations from satellites are available only since 2009 (Olmedo et al., 2021) and too short for the evaluation of the prediction skill. We find SSS and SC-700m predictability only in regions where salinity measurements are available over the whole assimilation period.

We analyze time series of area averaged SSS and SC-700m for the same North Atlantic region as for SST/HC-700m (60°W-10°W, 50°N-60°N). The time series of the observed North Atlantic SSS and SC-700m show a similar low-frequency signal as before with low values in the period 1970-1995 and high values thereafter (Fig. 5a, b). The amplitudes of the simulated SSS and SC-700m are larger than in the observations. For North Atlantic SSS the correlation values are 0.61 and 0.69 for ly1 and ly1-5, respectively. Additionally, for North Atlantic SC-700m the correlation values are 0.73 and 0.74 for ly1 and ly1-5, respectively.

The overview of the correlation values in the diagrams below the time series (Fig. 5c, d) show that for North Atlantic SSS, highest correlation values (cor=0.82) are present for ly1-9 and the correlation remains statistically significant up to ly6-9. For North Atlantic SC-700m the highest correlation value (cor=0.79) is present for ly3, ly2-2 and ly2-3 and the correlation is significant up to ly1-7 and ly5. The predictability in the North Atlantic region is important via its teleconnections for example for the European climate (e.g. Borchert et al., 2019).

3.2 Mean state and variability of AMOC

The long-term mean of the Atlantic Meridional Overturning Circulation (AMOC) of the assimilation run over the period 1960-2014 shows the expected structure (e.g. Jackson et al., 2019) with an upper cell with a maximum of 18 Sv (1 Sverdrup=106 m3 s-1) at about 25°N in 1000m depth and a weak counter-cell below (Fig. 6a). We show additionally the time series of AMOC at 26°N (Fig. 6b). The observed strength of the AMOC from the Rapid Climate Change Programme (RAPID) array (Moat et al., 2020) is of comparable strength. The AMOC from the assimilation has a positive trend in the 1960s and is thereafter relatively stable. However, the assimilation does not show the observed strength of the decline of more than 4 Sv around 2009. We argue that the overlap of only 12 years between the start of the observations in 2004 and the

end of ly1 of our hindcast in 2015 is too short for a robust estimate of the prediction skill. The Intergovernmental Report on Climate Change (IPCC) 6th assessment report (AR6; Arias et al., 2021) indicates that the AMOC at 30°N was relatively stable in the 20th century and is expected to decrease over the 21st century. That way, the relatively stable AMOC during the period 1970-2000 looks reasonable but we do not see signs of a decreasing AMOC in our hindcasts in the first two decades of the 21st century.

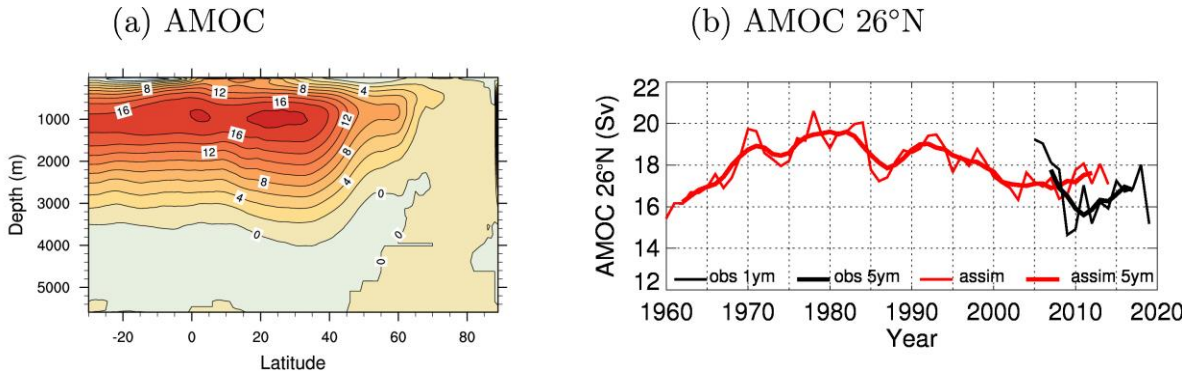

Figure 6. (a) Ensemble mean of the Atlantic meridional overturning circulation (AMOC) averaged over the period 1960-2014 from the assimilation. (b) Time series of ensemble mean AMOC anomalies at 26°N in 1000m depth from ICON-ESM hindcasts (red) and observations (RAPID, black).

3.3 Seasonal predictability of surface variables

We analyze the seasonal predictability as the average of lm2-4. Since we started our hindcasts on every 1 November, this represents the average over December, January and February (DJF). Table 1 gives an overview of the correlation values of the seasonal hindcasts against observations for different variables. The correlation of sea surface height (SSH) of the hindcasts with satellite observations from the Archiving, Validation and Interpretation of Satellite Oceanographic Data project (AVISO; Fablet et al., 2018) is high in the tropical Pacific and Indian Ocean (Fig. 7a). The correlation of surface temperature (TS, i.e. SST over the ocean and land surface temperature over land) with observations from Goddard Institute for Space Studies

Table 1. Overview about the seasonal boreal winter prediction skill values for the different variables, regions and periods (see text). Numbers in bold indicate significant values at the 95% level according to a t-test.

Variable	SSH	TS	Precipitation		SLP	
Region	NINO3.4	NINO3.4	East Pacific	West Pacific	Tahiti	Darwin
Period	1993-2015	1961-2015	1979-2015	1979-2015	1961-2015	1961-2015
Correlation	**0.80**	**0.79**	**0.82**	**0.72**	**0.55**	**0.59**
Reference	AVISO	GISTEMP	GPCP		HadSLP2	
Citation	Fablet et al., 2018	Lenssen et al., 2019	Adler et al., 2003		Allan & Ansell, 2006	

Surface Temperature Analysis (GISTEMP; Lenssen et al., 2019) is also high in these regions and additionally in large parts of the North Atlantic and North Pacific (Fig. 7b).

Our prediction system is capable of predicting El Niño/Southern Oscillation (ENSO) events on seasonal time-scales. Important for ENSO is the variability in the NINO3.4 region, representing averaged values in the region 170°W-120°W, 5°S-5°N. The NINO3.4 SSH hindcasts of boreal winter (DJF) largely agree with satellite observations (cor=0.80, Fig. 7c). The agreement of the NINO3.4 SST anomalies with observations from GISTEMP also lies in this range (cor=0.79, Fig. 7d). The prediction skill from other models is usually in the range of cor=0.90 for the shorter period from 1980-2001 (Jin et al., 2008). Our NINO3.4 SST prediction lies also in this range for the shorter period (cor=0.89).

Next, we analyze some atmospheric variables that are associated with ENSO. The correlation of precipitation of the hindcasts with observations from the Global Precipitation Climatology Project (GPCP; Adler et al., 2003) is significantly positive only in relatively small regions in the East and West Pacific (Fig. 8a). ENSO teleconnections are biased in ICON-ESM in particular at the equator (Jungclaus et al., 2022). We define an East Pacific precipitation index as the average over the region 160°E-90°W, 10°S-10°N. The precipitation anomalies of the hindcasts in the East Pacific correspond with observations in this region and season (cor=0.82, Fig. 8c). We also

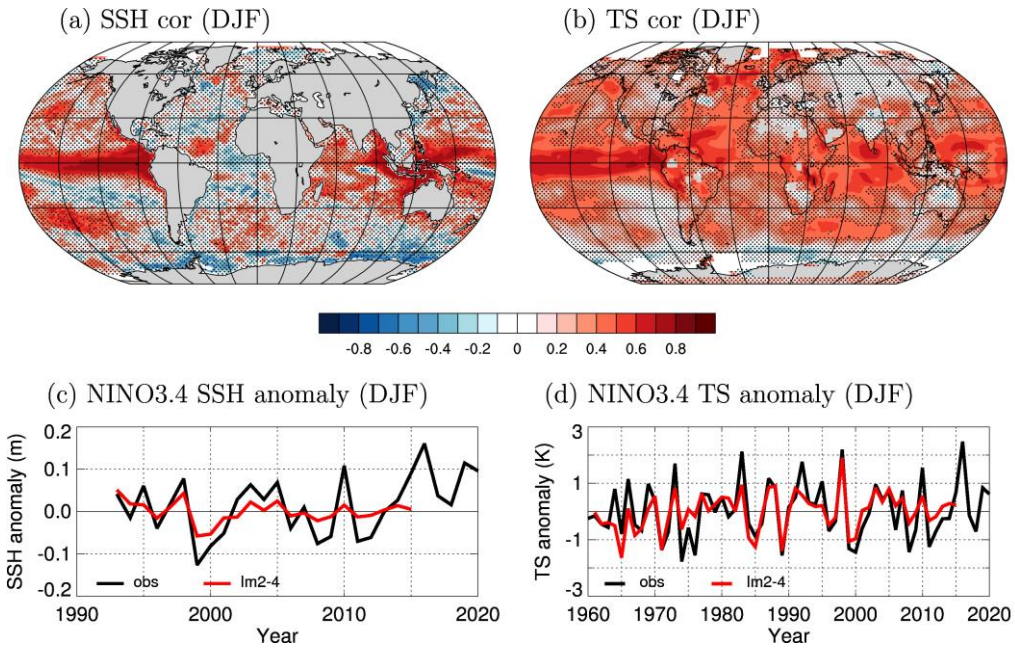

Figure 7. Correlation of (a) sea surface height (SSH) and (b) surface temperature (TS) from the ICON-ESM hindcasts with observations (AVISO and GISTEMP, respectively) for lead-month 2-4 (DJF). The correlations are based on averages of 10 ensemble members over the periods (a) 1993-2015 and (b) 1961-2015. Stippling indicates regions with non-significant values at the 95% level according to a t-test. (c, d) Time series of (c) SSH and (d) TS anomalies in the NINO3.4 region (5°S-5°N, 170°-120°W) from observations (AVISO and GISTEMP, respectively, black) and ICON-ESM hindcasts (red).

define a West Pacific precipitation index as the average over the region 110°E-140°E, 5°N-25°N. The West Pacific precipitation anomalies of the hindcasts agree also well with observations in this region and season (cor=0.72, Fig. 8e).

For sea level pressure (SLP), we find high correlation values of the hindcasts against observations from the Hadley Centre Sea Level Pressure dataset (HadSLP2; Allan & Ansell, 2006) in the East Pacific and West Pacific/Indian Ocean (Fig. 8b). The two regions are associated with the Southern Oscillation Index (SOI). We show two times series for SLP. We define the SLP index near Tahiti as the average over the region 145°W-155°W, 0°-20°S. The correlation of the Tahiti SLP data with observations is statistically significant (cor=0.55, Fig. 8d). We define the SLP index near Darwin as the average over the region 125°E-135°E, 0°-15°S.

293 The positive correlation of the Darwin SLP data with observations is also statistically significant
294 (cor=0.59, Fig. 8f).
295

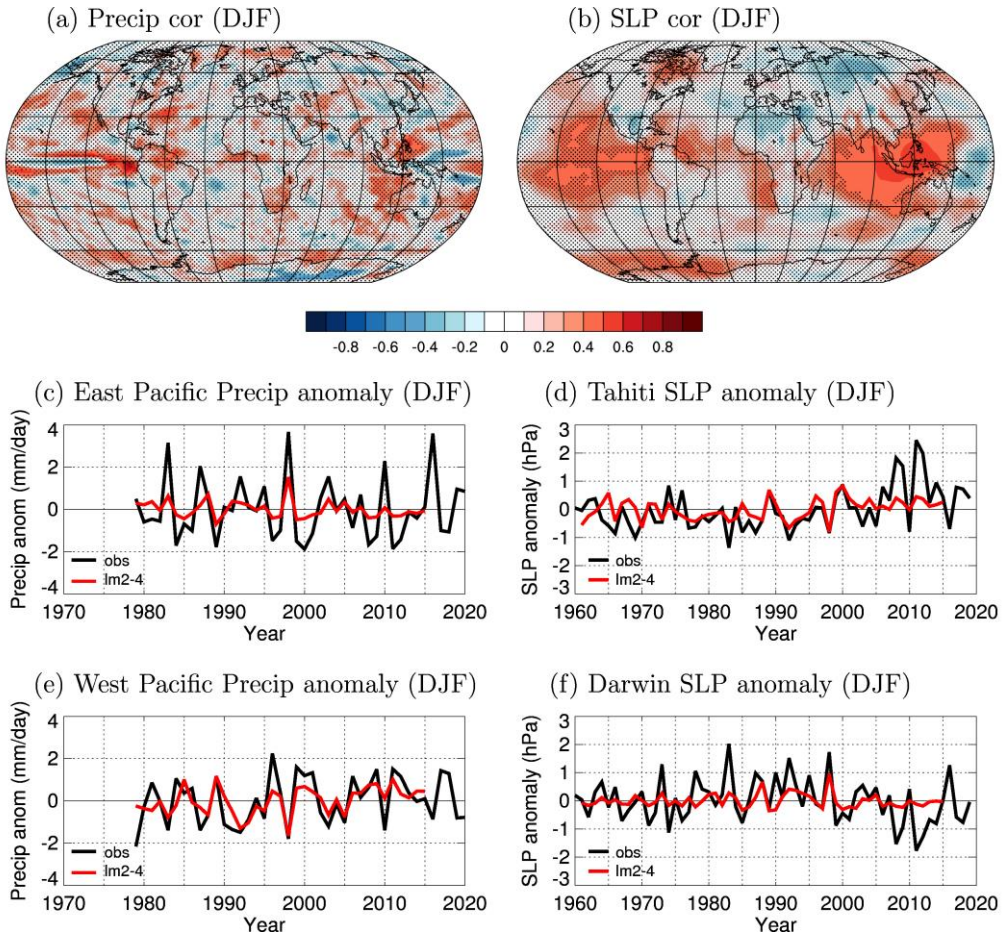

Figure 8. Correlation of (a) precipitation (Precip) and (b) sea level pressure (SLP) from the ICON-ESM hindcasts with observations (GPCP and HadSLP2, respectively) for lead-month 2-4 (DJF). The correlations are based on averages of 10 ensemble members over the periods (a) 1979-2015 and (b) 1961-2015. Stippling indicates regions with non-significant values at the 95% level according to a t-test. (c, d) Time series of Precip anomalies in the (c) East Pacific (5°S-5°N, 170°-120°W) and (d) West Pacific (5°S-5°N, 170°-120°W) from observations (black) and ICON-ESM hindcasts (red). (e, f) Time series of SLP anomalies near (c) Tahiti (5°S-5°N, 170°-120°W) and (f) Darwin (5°S-5°N, 170°-120°W) from observations (black) and ICON-ESM hindcasts (red).

296 **3.4 Mean state and predictability of sea ice**

297 We show averages of the Arctic and Antarctic sea ice concentration (SIC) as the mean over the
298 period 1979-2014 together with the sea ice extent (SIE, i.e. the area with at least 15% SIC) from
299 the assimilation and observations from HadISST (Rayner et al., 2003) in the respective summer

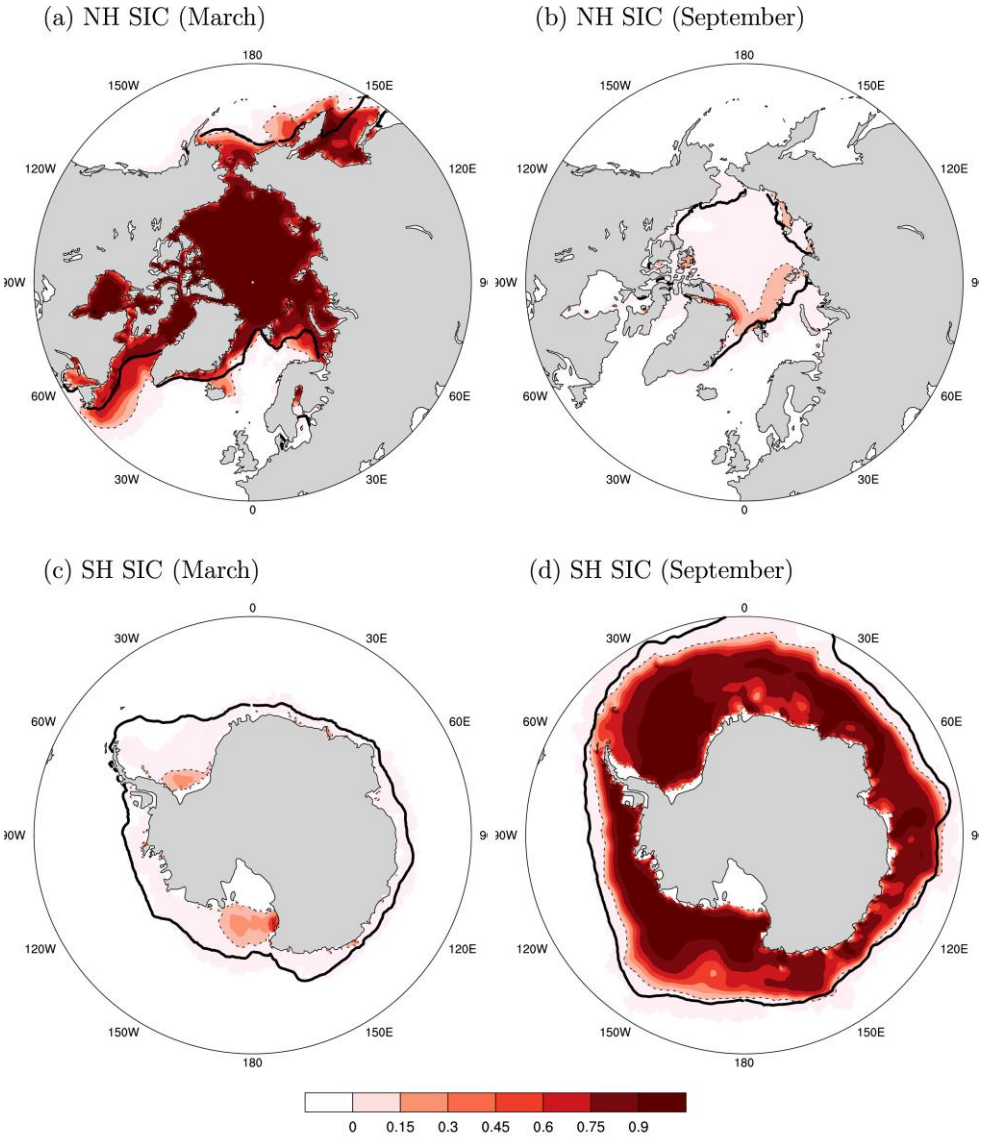

Figure 9. Mean sea ice concentration (SIC) of the assimilation averaged over the period 1979-2014 in the (a, b) Northern Hemisphere (NH) and (c, d) Southern Hemisphere in (a, c) March and (b, d) September (colored). A dashed and full line indicates the sea-ice extent (area with at least 15% ice-concentration) from the assimilation and observations, respectively.

and winter (Fig. 9). In the respective winter, the long-term mean of the SIE from the assimilation run shows relatively good agreement with observations in both hemispheres (Fig. 9a, d). In the Arctic, positive deviations from the observed long-term mean SIE are present in the Labrador and Bering Seas in winter (Fig. 9a). In the Antarctic, negative deviations from the observed SIE climatology are present almost circumpolar in winter (Fig. 9d). In summer, the SIE is much too low compared with observations in both hemispheres (Fig. 9b, c). In the Arctic, regions with SIC exceeding the 15% threshold can only be found in a relatively small area at the north coast of Greenland and extending further east, whereas in observations the Arctic remains almost completely ice covered in summer. In the Antarctic, regions with SIC exceeding the 15% threshold are limited to small areas in the Ross and Weddell Seas, while the observed sea ice cover remains much larger in summer. The sea ice biases in our assimilation experiment are similar to the biases in the ICON-ESM historical simulations (Jungclaus et al., 2022).

We analyze the SIE correlation of the hindcasts with observations from the National Snow and Ice Data Center (NSIDC; Fetterer et al., 2017) for the months with maximum and minimum SIE (i.e. March and September). Since our hindcasts are started on every 1 November this is for lead month 5 (March) and 11 (September), respectively. Table 2 gives an overview of the correlation values of the hindcasts against observations. The correlation of SIE of the hindcasts with observations is significantly positive only in the Northern Hemisphere in both seasons, summer and winter, due to the agreement of the decreasing trend. For winter (NH, March), the strength of the trend agrees with the observed trend (Fig. 10a), but in summer (NH, September), the hindcasts underestimate the trend possibly due to the general underestimation of the SIE during this season (Fig. 10b). This may also be the reason for the missing variability of SIE in the SH in

Table 2. Overview about the prediction skill values of sea ice extent (SIE) for the Northern Hemisphere (NH) and Southern Hemisphere (SH) in winter and summer against observations from NSIDC (Fetterer et al., 2017) over the period 1979-2015.

Variable	SIE			
Region	NH		SH	
Season (Month of minimum and maximum)	March (Winter)	September (Summer)	March (Summer)	September (Winter)
Correlation	**0.80**	**0.80**	-0.34	-0.24

summer (Fig. 10c). In winter in the SH, the SIE trend of the hindcasts agrees with the observed trend only in the later period from the late 1990s (Fig. 10d). This may be also due to general problems with simulated variability in the Southern Ocean, e.g. the Antarctic circumpolar current is too weak in ICON-ESM compared to observations (Jungclaus et al., 2022).

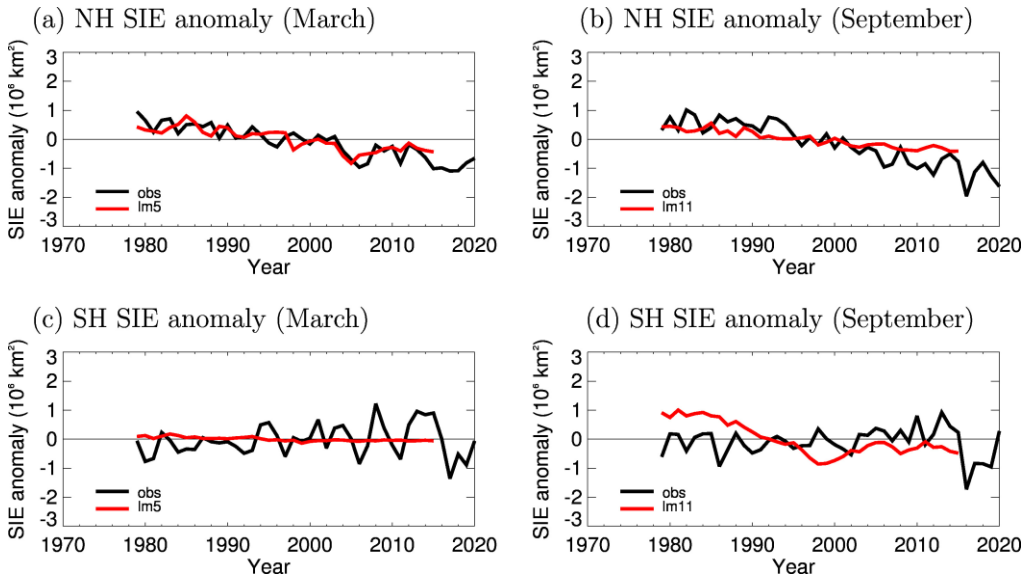

Figure 10. Time series of sea ice extent (SIE) anomalies in the (a, b) Northern Hemisphere (NH) and (c, d) Southern Hemisphere (SH) in (a, c) March and (b, d) September from observations (NSIDC, black) and the hindcasts from ICON-ESM for lead months (a, c) 5 and (b, d) 11 (red).

4 Discussion and summary

We developed an oceanic initialization technique based on the PDAF EnKF as a first step towards a weakly coupled data assimilation in ICON-ESM. We performed an assimilation run over the period 1960-2014. The assimilation serves to initialize decadal hindcasts started on 1 November in each year. In general, the PADF EnKF successfully assimilates oceanic temperature and salinity profile observations into ICON-ESM. With our approach of initializing only the oceanic part, we find - largely in agreement with expectations - high predictive skill in the following variables and regions:

We find multi-annual predictability of SST, SSS, HC700m and SC-700m especially in the North Atlantic. Additionally, seasonal predictability is present in the tropics with highest values in variables related to ENSO. We find high predictive skill of SST and SSH especially in the tropical Pacific (ENSO) implicating a high predictive skill for precipitation and SLP in this region. ENSO predictability lies in the range of other models for DJF. However, compared to other prediction systems, prediction skill is relatively low in regions apart from the tropical Pacific due to the missing atmospheric assimilation. Additionally, the hindcasts correctly represent the decreasing SIE trend in the Arctic in winter and to a lesser degree also in summer although the mean SIE in ICON-ESM is much too low in summer in both hemispheres. This, and additional general problems with simulating the variability in the Southern Ocean, causes the mismatch between simulated and observed SIE in the Antarctic in winter and summer.

We have used the ICON-ESM in our prediction system in relatively low resolution compared to other systems. However, the advantage of ICON is its good performance at high resolution due to the scalability of the code and the use of non-hydrostatic equations for the atmosphere that allow high resolution convection permitting simulations (Stevens et al., 2019). Another advantage is the availability of adaptive grids as well for the atmosphere (Maurer et al., 2022) as for the ocean (Logemann et al., 2021). The role of such improvements for seasonal and near-term predictions will be investigated in forthcoming studies.

In general, we can confirm that our data assimilation method is successfully initializing the oceanic component of the climate system. We expect that the second step towards a weakly coupled data assimilation - an additional atmospheric assimilation - will enhance the prediction skill further and will lead to high quality seasonal and decadal climate predictions. An additional fine-tuning of the climate model could also improve the prediction skill, e.g. with a more realistic Arctic and Antarctic sea ice climatology in summer and an improved oceanic circulation in the Southern Ocean. We are currently restructuring the ICON code by unifying the physical parameterization packages for numerical weather preditions and climate applications. The ICON-seamless project is working on advancing all aspects of the coupled climate system

(atmosphere, land, ocean, cryosphere and data assimilation) for improved weather and climate predictions on time sclaes from days to centuries.

Acknowledgments

HP and CS received funding from DWD's "Innovation Programme for Applied Researches and Developments" IAFE DAKLIM VH 3.5 and IAFE GCFS3.0, respectively. JB and SB were supported by Copernicus Climate Change Service, funded by the EU, under contract C3S-330 and C3S2-370. JHJ acknowledges support from the Collaborative Research Centre TRR 181 "Energy Transfers in Atmosphere and Ocean" funded by the Deutsche Forschungsgemeinschaft (DFG, German Research Foundation - Project Number 274762653). This work used resources of the Deutsches Klimarechenzentrum (DKRZ) granted by its Scientific Steering Committee (WLA) under project ID uo1075.

Data availability statement

The model code of ICON is available to individuals under licenses https://mpimet.mpg.de/en/science/modeling-with-icon/code-availability (accessed 2021-12-10). By downloading the ICON source code, the user accepts the license agreement. The source code of the ICON-ESM-V1.0 used in this study, primary data, and scripts used in the analyses and for producing the figures can be obtained from Zenodo (https://doi.org/10.5281/zenodo.6034081). The data from the ICON-ESM simulations can be accessed from the DKRZ via https://cera-www.dkrz.de/WDCC/ui/cerasearch/entry?acronym=DKRZ_LTA_1075_ds00009. We have used ncl-scripts from DKRZ https://www.dkrz.de/up/services/analysis/visualization/sw/ncl/ncl-examples (accessed 2021-12-16). PDAF (Nerger & Hiller, 2013) is available at the PDAF website http://pdaf.awi.de (accessed 2020-01-16). EN.4.2.1 data (Good et al., 2004) were obtained from https://www.metoffice.gov.uk/hadobs/en4/ (accessed 2018-01-19) and are © British Crown Copyright, Met Office, 2021, provided under a Non-Commercial Government License http://www.nationalarchives.gov.uk/doc/non-commercial-government-licence/version/2/ The HadISST data set (Rayner et al., 2003) was downloaded from https://www.metoffice.gov.uk/hadobs/hadisst (accessed 2021-12-10). The subsurface

temperature and salinity analyses (Ishii et al., 2005) were downloaded from the research data archive at the National Center for Atmospheric Research, Computational and Information Systems Laboratory from https://rda.ucar.edu/dataset/ds285.3 (accessed 2022-02-02). Data from the RAPID AMOC monitoring project (Moat et al., 2020) is funded by the Natural Environment Research Council and are freely available from www.rapid.ac.uk/rapidmoc (accessed 2021-12-05). AVISO data (Fablet et al., 2018) were processed by SSALTO/DUACS and distributed by AVISO+ (https://www.aviso.altimetry.fr) with support from CNES. The AVISO data set SEALEVEL_GLO_PHY_L4_REP_OBSERVATIONS_008_047 was downloaded from https://resources.marine.copernicus.eu (accessed 2021-12-10). The following data are provided by NOAA/OAR/ESRL PSL, Boulder, Colorado, USA: GPCP precipitation data (Adler et al., 2003) are obtained from https://psl.noaa.gov/data/gridded/data.gpcp.html (accessed 2021-12-10). GISTEMPv4 data (Lenssen et al., 2019) were downloaded from https://downloads.psl.noaa.gov/Datasets/gistemp/combined/250km/air.2x2.250.mon.anom.comb.nc (accessed 2021-12-10). The HadSLP2 data (Allen & Ansell, 2006) are obtained from https://psl.noaa.gov/data/gridded/data.hadslp2.html (accessed 2021-12-10). NSIDC Sea ice extent data (Fetterer et al., 2017) are downloaded from https://psl.noaa.gov/data/timeseries/monthly/SHICE/ and https://psl.noaa.gov/data/timeseries/monthly/NHICE/ (accessed 2021-12-10).

References

Adler, R. F., Huffman, G. J., Chang, A., Ferraro, R., Xie, P.-P., Janowiak, J., et al. (2003), The Version 2 Global Precipitation Climatology Project (GPCP) Monthly Precipitation Analysis (1979-Present). *Journal of Hydrometeorology*, *4*, 1147–1167. https://doi.org/10.1175/1525-7541(2003)004<1147:TVGPCP>2.0.CO;2

Allan, R., & Ansell, T. (2006), A new globally complete monthly historical mean sea level pressure data set (HadSLP2): 1850-2004. *Journal of Climate*, *19*, 5816–5842. https://doi.org/10.1175/JCLI3937.1

Arias, P. A., Bellouin, N., Coppola, E., Jones, R. G., Krinner, G., Marotzke, J., et al. (2021), Technical Summary. In Climate Change 2021: The Physical Science Basis. Contribution of Working Group I to the Sixth Assessment Report of the Intergovernmental Panel on Climate Change [Masson-Delmotte, V., P. Zhai, A. Pirani, S. L. Connors, C. Péan, S. Berger, N. Caud, Y. Chen, L. Goldfarb, M. I. Gomis, M. Huang, K. Leitzell, E. Lonnoy, J. B. R. Matthews, T. K. Maycock, T. Waterfield, O. Yelekçi, R. Yu, and B. Zhou (eds.)]. *Cambridge University Press*. In Press. https://www.ipcc.ch/report/ar6/wg1/downloads/report/IPCC_AR6_WGI_TS.pdf

Athanasiadis, P. J., Yeager, S., Kwon, Y.-O., Bellucci, A., Smith, D. W., & Tibaldi, S. (2020), Decadal predictability of North Atlantic blocking and the NAO. *npj Climate and Atmospheric Science*, *3*, 20. https://doi.org/10.1038/s41612-020-0120-6

Boer, G. J., Smith, D. M., Cassou, C., Doblas-Reyes, F., Danabasoglu, G., Kirtman, B., et al. (2016), The Decadal Climate Prediction Project (DCPP) contribution to CMIP6, *Geoscientific Model Development*, *9*, 3751–3777, https://doi.org/10.5194/gmd-9-3751-2016

Borchert, L. F., Pohlmann, H., Baehr, J., Neddermann, N.-C., Suarez-Gutierrez, L., & Müller, W. A. (2019), Decadal predictions of the probability of occurrence for warm summer temperature extremes. *Geophysical Research. Letters*, *46*, 14042–14051. https://doi.org/doi:10.1029/2019GL085385

Brune, S., Nerger, L., & Baehr, J. (2015), Assimilation of oceanic observations in a global coupled Earth system model with the SEIK filter. *Ocean Modelling*, 96, 254–264. https://doi.org/10.1016/j.ocemod.2015.09.011

Brune, S., Düsterhus, A., Pohlmann, H., Müller, W. A., & Baehr, J. (2018), Time dependency of the prediction skill for the North Atlantic subpolar gyre in initialized decadal hindcasts. *Climate Dynamics*, *51*, 1947–1970. https://doi.org/10.1007/s00382-017-3991-4

Brune, S., & Baehr, J. (2020), Preserving the coupled atmosphere-ocean feedback intinitializations of decadal climate predictions. *WIREs Climate Change, 11,* e637. https://doi.org/10.1002/wcc.637

Crueger, T., Giorgetta, M. A., Brokopf, R., Esch, M., Fiedler, S., Hohenegger, C., et al. (2018), ICON-A, the atmosphere component of the ICON Earth system model: II. Model evaluation. *Journal of Advances in Modeling Earth Systems, 10,* 1638–1662. https://doi.org/10.1029/2017MS001233

Dunstone, N. J., & Smith, D. M. (2010), Impact of atmosphere and sub-surface ocean data on decadal climate prediction. *Geophysical Research Letters, 37,* L02709. https://doi.org/10.1029/2009GL041609

Eyring, V., Bony, S., Meehl, G. A., Senior, C. A., Stevens, B., Stouffer, R. J., & Taylor, K. E. (2016), Overview of the Coupled Model Intercomparison Project Phase 6 (CMIP6) experimental design and organization. *Geoscientific Model Development, 9,* 1937–1958. https://doi.org/10.5194/gmd-9-1937-2016

Fablet, R., Verron, J., Mourre, B., Chapron B., & Pascual, A. (2018), Improving Mesoscale Altimetric Data From a Multitracer Convolutional Processing of Standard Satellite-Derived Products. *IEEE Transactions on Geoscience and Remote Sensing, 56, 5,* 2518–2525. https://doi.org/10.1109/TGRS.2017.2750491

Fetterer, F., Knowles, K., Meier, W., Savoie, M., & Windnagel, A. K. (2017), updated daily. Sea Ice Index, Version 3. Boulder, Colorado USA. NSIDC: National Snow and Ice Data Center. https://doi.org/10.7265/N5K072F8

Fröhlich, K., Dobrynin, M., Isensee, K., Gessner, C., Paxian, A., Pohlmann, H., et al. (2021), The German climate forecast system: GCFS. *Journal of Advances in Modeling Earth Systems, 13,* e2020MS002101. https://doi.org/10.1029/2020MS002101

Giorgetta, M. A., Brokopf, R., Crueger, T., Esch, M., Fiedler, S., Helmert, J., et al. (2018), ICON-A, the atmosphere component of the ICON Earth system model: I. Model description. *Journal of Advances in Modeling Earth Systems, 10,* 1613–1637. https://doi.org/10.1029/2017MS001242

Good, S. A., Martin, M. J., & N. A. Rayner, N. A. (2013), EN4: Quality controlled ocean temperature and salinity profiles and monthly objective analyses with uncertainty estimates. *Journal of Geophysical Research: Oceans, 118,* 6704–6716. https://doi.org/10.1002/2013JC009067

Hanke, M., Redler, R., Holfeld, T., & Yastremsky, M. (2016), YAC 1.2.0: new aspects for coupling software in Earth system modeling. *Geoscientific Model Development, 9,* 2755–2769. https://doi.org/10.5194/gmd-9-2755-2016

Hermanson, L., Smith, D., Seabrook, M., Bilbao, R., Doblas-Reyes, F., Tourigny, E., et al. (2022), WMO Global Annual to Decadal Climate Update: A prediction for 2021-2025. *Bulletin of the American Meteorological Society,* accepted

Ishii, M., Kimoto, M., Sakamoto, K., & Iwasaki, S. (2005), Subsurface temperature and salinity analyses. Research Data Archive at the National Center for Atmospheric Research, Computational and Information Systems Laboratory. https://doi.org/10.5065/Y6CR-KW66

Ishii, M., Kimoto, M., Sakamoto, K., & Iwasaki, S. I. (2006), Steric sea level changes estimated from historical ocean subsurface temperature and salinity analyses. *Journal of Oceanography, 62(2),* 155–170. https://doi.org/10.1007/s10872-006-0041-y

Jackson, L. C., Dubois, C., Forget, G., Haines, K., Harrison, M., Iovino, D., et al. (2019), The mean state and variability of the North Atlantic circulation: A perspective from ocean reanalyses. *Journal of Geophysical Research: Oceans, 124,* 9141–9170. https://doi.org/10.1029/2019JC015210

519 Jin, E. K., Kinter, J. L., Wang, B., Park, C.-K., Kang, I.-S., Kirtman, B. P., et al. (2008), Current
520 status of ENSO prediction skill in coupled ocean–atmosphere models. *Climate Dynamics, 31,*
521 647–664. https://doi.org/10.1007/s00382-008-0397-3
522
523 Jungclaus, J. H., Lorenz, S. J., Schmidt, H., Brovkin, V., Brüggemann, N., Chegini, F., et al.
524 (2022), The ICON Earth System Model Version 1.0. *Journal of Advances in Modeling Earth*
525 *Systems*, submitted. https://www.essoar.org/doi/10.1002/essoar.10507989.1
526
527 Keenlyside, N. S., Latif, M., Jungclaus, J., Kornblueh, L., & Roeckner, E. (2008), Advancing
528 decadal-scale climate prediction in the North Atlantic sector. *Nature 453,* 84–88.
529 https://doi.org/10.1038/nature06921
530
531 Korn, P. (2017), Formulation of an Unstructured Grid Model for Global Ocean Dynamics,
532 *Journal of Computational Physics, 339,* 525–552. https://doi.org/10.1016/j.jcp.2017.03.009
533
534 Kröger, J., Pohlmann, H., Sienz, F., Marotzke, J., Baehr, J., Köhl, A., et al. (2018), Full-field
535 initialized decadal predictions with the MPI earth system model: an initial shock in the North
536 Atlantic. *Climate Dynamics, 51,* 2593–2608. https://doi.org/10.1007/s00382-017-4030-1
537
538 Kushnir, Y., Scaife, A. A., Arritt, R., Balsamo, G., Boer, G., Doblas-Reyes, F, at al. (2019),
539 Towards operational predictions of the near-term climate. *Nature Climate Change, 9,* 94–101.
540 https://doi.org/10.1038/s41558-018-0359-7
541
542 Lenssen, N. J. L., Schmidt, G. A., Hansen, J. E., Menne, M. J., Persin, A., Ruedy, R., & Zyss, D.
543 (2019), Improvements in the GISTEMP uncertainty model. *Journal of Geophysical Research:*
544 *Atmospheres, 124,* 6307–6326. https://doi.org/10.1029/2018JD029522
545
546 Logemann, K., Linardakis, L., Korn, P., & Schrumm, C. (2021), Global tide simulations with
547 ICON-O: testing the model performance on highly irregular meshes. Ocean Dynamics, 71,43-57.
548 https://doi.org/10.1007/s10236-020-01428-7
549

Maerz, J., Six, K. D., Stemmler, I., Ahmerkamp, S., and Ilyina, T. (2020), Microstructure and composition of marine aggregates as co-determinants for vertical particulate organic carbon transfer in the global ocean. *Biogeosciences, 17*, 1765–1803, https://doi.org/10.5194/bg-17-1765-2020

Maurer, V., Früh, B., Giorgetta, M. A., Steger, C., Brauch J., Schnur, R., et al. (2022), Domain nesting in ICON and its application to AMIP experiments with regional refinement. J*ournal of Advances in Modeling Earth Systems*, submitted. https://www.essoar.org/doi/10.1002/essoar.10507778.1

Moat, B. I., Smeed, D. A., Frajka-Williams, E., Desbruyeres, D. G., Beaulieu, C., Johns, W. E., et al. (2020), Pending recovery in the strength of the meridional overturning circulation at 26°N. *Ocean Science, 16*, 863–874. https://doi.org/10.5194/os-16-863-2020

Nerger, L., & Hiller, W. (2013), Software for Ensemble-based Data Assimilation Systems - Implementation Strategies and Scalability. *Computers and Geosciences, 55*, 110–118. https://doi.org/10.1016/j.cageo.2012.03.026

Olmedo, E., Gonzales-Haro, C., Hoareau, N., Umbert, M., Gonzales-Gambau, V., Martinez, J., et al. (2021), Nine years of SMOS sea surface salinity global maps at the Barcelona Expert Center. Earth System Science Data, 13, 857–888. https://doi.org/10.5194/essd-13-857-2021

Pasternack, A., Bhend, J., Liniger, M. A., Rust, H. W., Müller, W. A., & Ulbrich, U. (2018), Parametric decadal climate forecast recalibration (DeFoReSt 1.0). *Geoscientific Model Development, 11*, 351–368. https://doi.org/10.5194/gmd-11-351-2018

Penny, S. G., Bach, E., Bhargava, K., Chang, C.-C., Da, C., Sun, L., & Yoshida, T. (2019), Strongly coupled data assimilation in multiscale media: Experiments using a quasi-geostrophic coupled model. *Journal of Advances in Modeling Earth Systems, 11*, 1803–1829. https://doi.org/10.1029/2019MS001652

Pham, D. T. (2001), Stochastic Methods for Sequential Data Assimilation in Strongly Nonlinear Systems. Monthly Weather Review, 129, 1194–1207. https://doi.org/10.1175/1520-0493(2001)129<1194:SMFSDA>2.0.CO;2

Pohlmann, H., Jungclaus, J. H., Köhl, A., Stammer, D., & Marotzke, J. (2009), Initializing decadal climate predictions with the GECCO oceanic synthesis: Effects on the North Atlantic. *Journal of Climate, 22,* 3926–3938. https://doi.org/10.1175/2009JCLI2535.1

Pohlmann, H., Müller, W. A., Bittner, M., Hettrich, S., Modali, K., Pankatz, K., & Marotzke, J. (2019), Realistic quasi-biennial oscillation variability in historical and decadal hindcast simulations using CMIP6 forcing. *Geophysical Research Letters, 46,* 14118–14125. https://doi.org/10.1029/2019GL084878

Polkova, I., Brune, S., Kadow, C., Romanova, V., Gollan, G., Baehr, J., et al. (2019), Initialization and ensemble generation for decadal climate predictions: A comparison of different methods. *Journal of Advances in Modeling Earth Systems, 11,* 149–172. https://doi.org/10.1029/2018MS001439

Rayner, N. A., Parker, D. E., Horton, E. B., Folland, C. K., Alexander, L. V., Rowell, D. P., et al. (2003), Global analyses of sea surface temperature, sea ice, and night marine air temperature since the late nineteenth century. *Journal of Geophysical Research, 108, D14,* 4407. https://doi.org/10.1029/2002JD002670

Reick, C. H., Gayler, V., Goll, D., Hagemann, S., Heidkamp, M., Nabel, J. E. M. S., et al. (2021), JSBACH 3 - The land component of the MPI Earth System Model: Documentation of version 3.2. *Berichte zur Erdsystemforschung,* 240. https://doi.org/10.17617/2.3279802

Smith, D. M., Eade, R., Scaife, A. A., Caron, L.-P., Danabasoglu, G., DelSole, T. M., et al. (2019), Robust skill of decadal climate predictions. *npj Climate and Atmospheric Science, 2,* 13. https://doi.org/10.1038/s41612-019-0071-y

Stevens, B., Satoh, M., Auger, L., Biercamp, J., Bretherton, C. S., Chen, X., et al. (2019), DYAMOND: the DYnamics of the Atmospheric general circulation Modeled On Non-hydrostatic Domains. *Progress in Earth and Planetary Science, 6,* 61. https://doi.org/10.1186/s40645-019-0304-z

Swingedouw, D., Mignot, J., Labetoulle, S., Guilyardi, E., & Madec, G. (2013), Initialisation and predictability of the AMOC over the last 50 years in a climate model. *Climate Dynamics, 40,* 2381–2399. https://doi.org/10.1007/s00382-012-1516-8

Taylor, K. E., Stouffer, R. J., & Meehl, G. A. (2012), An Overview of CMIP5 and the Experiment Design. *Bulletin of the American Meteorological Society, 93(4),* 485–498. https://doi.org/10.1175/BAMS-D-11-00094.1

Thoma, M., Greatbatch, R. J., Kadow, C., & Gerdes, R. (2015), Decadal hindcasts initialized using observed surface wind stress: Evaluation and prediction out to 2024, *Geophysical Research Letters, 42,* 6454–6461. https://doi.org/10.1002/2015GL064833

Tompkins, A. M., de Zarate, M. I., Saurral, R. I., Vera, C., Saulo, C., Merryfield, W. J., et al. (2017), The climate-system historical forecast project: Providing open access to seasonal forecast ensembles from centers around the globe. *Bulletin of the American Meteorological Society, 98,* 2293–2301. https://doi.org/10.1175/BAMS-D-16-0209.1

Wilks, D. S. (2011), Statistical methods in the atmospheric sciences, 3rd edn. International geophysics series, Vol 100. *Academic Press, Elsevier, Amsterdam, The Netherlands*. ISBN: 9780123850225

Zängl, G., Reinert, D., Ripodas, P., & Baldauf, M. (2015), The ICON (ICOsahedral Non-hydrostatic) modelling framework of DWD and MPI-M: Description of the non-hydrostatic dynamical core. *Quarterly Journal of the Royal Meteorological Society, 141,* 563–579. https://doi.org/10.1002/qj.2378